Materials Today Nano 24 (2023) 100382

Contents lists available at ScienceDirect

Materials Today Nano

journal homepage: www.sciencedirect.com/journal/materials-today-nano

Temperature-dependent photoconductivity in two-dimensional MoS_2 transistors

A. Di Bartolomeo [a,b,*], A. Kumar [a], O. Durante [a,b], A. Sessa [a], E. Faella [a,b], L. Viscardi [a,b], K. Intonti [a,b], F. Giubileo [b], N. Martucciello [b], P. Romano [b,c], S. Sleziona [d], M. Schleberger [d]

[a] Department of Physics 'E.R. Caianiello', University of Salerno, Via Giovanni Paolo II 132, Fisciano 84084, Italy
[b] CNR-SPIN Salerno, Via Giovanni Paolo II 132, Fisciano 84084, Italy
[c] Dipartimento di Scienze e Tecnologie, Università Del Sannio, Via de Sanctis, Benevento 82100, Italy
[d] Fakultät für Physik and CENIDE, Universität Duisburg-Essen, Lotharstrasse 1, Duisburg D-47057, Germany

ARTICLE INFO

Keywords:
MoS_2
Photoconductivity
Adsorbates
Photogating effect
Temperature
Pressure
Field effect transistors

ABSTRACT

The photoconductivity in monolayer MoS_2 back-gate transistors is studied as a function of temperature and pressure. The photocurrent increases linearly with the light intensity up to a maximum responsivity of ~30 A/W in air. Time-resolved photocurrent measurements confirm that the photoresponse is dominated by the photogating effect. The device shows slow photoresponse with two-time constants that are attributed to the photobolometric effect and the desorption of adsorbates, respectively. An enhancement of the photocurrent is observed above room temperature and below the atmospheric pressure, that is, when the photoinduced desorption of adsorbates such as O_2 and H_2O molecules is facilitated. Indeed, the light-induced removal of adsorbates from the surface of MoS_2 enhances the n-doping level and the current of the channel. Moreover, at lower pressures, the reverse mechanism of re-adsorption in dark conditions is suppressed and results in a persistent photocurrent. The study clarifies the photocurrent relaxation dynamics and unveils the key role of surface adsorbates in the optoelectronic properties of monolayer MoS_2 and other similar 2D materials.

1. Introduction

Molybdenum disulfide (MoS_2) has been the most studied two-dimensional (2D) material after graphene. The monolayer MoS_2 has an hexagonal lattice with covalently bonded S–Mo–S atoms arranged in a sandwiched structure with a nominal thickness of 0.65 nm and (1.8–1.9) eV direct bandgap [1,2]. A transition from direct-to-indirect bandgap and a bandgap reduction is observed while increasing the number of layers. The bandgap becomes 1.2 eV in the bulk material, where stacked layers are held together by weak van der Waals forces [3].

MoS_2 is a native n-type material, mainly due to omnipresent electron-donating sulfur vacancies [4–8]. However, the doping level and conductivity can be strongly modulated by the environment, making monolayer MoS_2 an outstanding material for chemical and biological sensors [9–12]. MoS_2 is also a good candidate for post-silicon electronic devices as it enables ultrathin field effect transistors (FETs) with on/off current ratios up to 10^8, subthreshold swing close to the theoretical limit of 60 mV/decade, and mobility around 200 $cm^2/V/s$ at room temperature [13]. The direct bandgap combined with the excitonic nature is at the origin of a strong light–matter interaction that results in a high absorption coefficient of ~10^6/cm, that is, about one order of magnitude higher than the absorption coefficient of Si and GaAs [14–16]. The optical absorption of visible light by monolayer MoS_2 is dominated by the direct transition from the valence to the conduction band (A exciton peak around 1.86 eV), while the excitonic nature manifests in extra absorption peaks like the B peak around 2.0 eV [17–19].

Owing to the strong light absorption and the excellent mechanical properties [20], monolayer MoS_2 has been identified as an ideal material for ultrathin and flexible photodetectors, with relatively high light conversion efficiency, despite the thin thickness [21,22]. Moreover, the short electron–hole and exciton lifetimes in monolayer MoS_2, which are largely independent of the temperature, can enable photodetectors with fast intrinsic temporal response. MoS_2 photodetectors with intrinsic response times as short as 3 ps, implying photodetection bandwidths as wide as 300 GHz, have been demonstrated [23]. However, the dynamics associated with photogenerated carriers are strongly affected by gap states and the environment. Hence, the photoresponse of MoS_2-based devices can show a non-unique behavior. For instance, slow or persistent

* Corresponding author.
E-mail address: adibartolomeo@unisa.it (A. Di Bartolomeo).

https://doi.org/10.1016/j.mtnano.2023.100382
Received 17 April 2023; Received in revised form 11 July 2023; Accepted 18 July 2023
Available online 24 July 2023

photocurrents, with rise and decay times of several dozen to several thousand seconds, are typically measured in back-gate phototransistors [24–28]. The slow photoresponse is attributed to the presence of intrinsic and extrinsic defects that act as charge-trapping centers [27] and to environmental effects [29]. The key role of adsorbates, such as O_2 and H_2O, that can be desorbed under illumination, increasing the n-doping and the conductivity of MoS_2, has been also recognized [30–33]. Under illumination, photogenerated holes discharge the negative molecules through surface electron–hole recombination, which are consequently easily photodesorbed from the surface. Remarkably, adsorbed O_2 and H_2O molecules have been identified as the main cause of the negative photoconductivity observed in n-type MoS_2 as well as in p-type 2D materials like $PtSe_2$ [34–37].

Charge trapping in intrinsic or extrinsic defects of MoS_2 or chemi- or physisorbed adsorbates at the MoS_2 surface can generate the so-called photogating effect that manifests as a shift of the transfer characteristics and a variation of the threshold voltage with consequent increase in the FET current [26]. Under illumination, the photogating effect causes a slow photoresponse ($\sim$ 10–100 s) that sometimes overcomes the faster photoconductive effect arising from the collection of photogenerated electron–hole pairs [26,29,38].

Due to the complexity of the involved processes, the photoresponse of monolayer MoS_2 can be difficult to interpret and requires great attention [39]. A study of the photocurrent under controlled temperature and pressure can help to distinguish among different mechanisms, such as, for instance, the role of trap centers and adsorbates. Moreover, the dependence of the photoresponse on environmental conditions is a prerequisite for the application of MoS_2-based photodetectors under extreme conditions, such as those encountered in aerospace. Despite its fundamental and practical importance, the dependence of photoconductivity on temperature and pressure has been only partially investigated. To fill the gap, herein, we study the photoconductivity in monolayer MoS_2 at different temperatures and pressures. We show that the time-resolved photocurrent is negligibly contributed by directly photogenerated electron–hole pairs collected at the electrodes but is instead dominated by the slow photobolometric effect and the slower photogating effect. The photobolometric effect results in the release of electrons from shallow traps, such as sulfur vacancies, under the heating induced by photon absorption, while the photogating effect is caused by positive charges trapped in intragap levels and the desorption of polar adsorbates [40]. More importantly, we find that the photocurrent is enhanced while increasing the temperature from room temperature to 370 K as well as while decreasing the pressure from atmospheric pressure down to 10^{-5} mbar. The effect of pressure has been widely discussed, also in the context of hysteresis in the FET's transfer characteristics [7,41]. Conversely, the temperature behavior of photoconductivity in 2D materials has been rarely reported and discussed in the literature.

In the attempt to obtain insights into the dynamics of the trap centers that had been invoked to explain a persistent photoconductivity [38], Zhang and co-workers investigated the temperature dependence of monolayer MoS_2 photoconductivity in the temperature range of 300 K–4.2 K through steady-state and time-resolved photocurrent measurements in vacuum [42]. They observed that the steady-state photocurrent decreases from 300 K to 153 K and then becomes weakly dependent on the temperature. They attributed such behavior to trapping/detrapping of the photogenerated carriers by traps associated with localized defect states dominated by the long-range Coulomb potentials at the SiO_2/-MoS_2 interface. Since these traps are thermally activated, the temperature dependence of the photocurrent becomes more prominent toward higher temperatures, while the carriers from trap states are frozen and do not contribute to the photocurrent at lower temperatures [42]. Pulikodan et al. investigated the photoresponse of a film of solution-processed few-layer MoS_2 nanosheets via time-resolved photocurrent measurements in two terminal devices, showing that the film exhibited a fast response followed by a slow-rise current under continuous illumination [40]. They attributed the slow-rise current effects to photobolometric and trap-assisted photogating processes and highlighted a correlation of the slow-rise current with the vacuum level and the temperature in the 11–310 K range. Gustafson and co-workers looked at the effect of temperature on the persistent photoconductivity of monolayer MoS_2 in 760 Torr of O_2 at 300 K, 230 K, and 160 K [43]. They found that the long-lived photoconductivity decreases as the temperature decreases, a behavior that they ascribed to photoinduced oxygen desorption. When the temperature decreases, fewer oxygen molecules desorb from the surface of the MoS_2 upon photoexcitation; thus, fewer electrons transfer back to the MoS_2 causing a reduction of persistent photoconductivity [43].

Herein, as a complement to previous works, we systematically investigate the temperature behavior of MoS_2 photocurrent above room temperatures, both in vacuum and air, using monolayer MoS_2 single flakes. We show that the temperature-enhanced photoconductivity can be explained by thermally assisted photoinduced desorption of O_2 and H_2O molecules from the MoS_2 surface that enhances the n-type doping and therefore the conductivity of the MoS_2 flake. This study clarifies the photocurrent relaxation dynamics and the role of surface adsorbates in the optoelectronic properties of monolayer MoS_2 flakes and other similar 2D materials.

2. Results and discussion

2.1. Device fabrication

MoS_2 flakes were grown via chemical vapor deposition (CVD) on a highly doped p-type Si substrate covered by 285 nm thermal SiO_2. Fig. 1a shows an atomic force microscope (AFM) image of a typical flake just after the growth process; the height profile in Fig. 1b indicates a thickness of about 0.9 nm corresponding to a monolayer [13,44]. The MoS_2 flakes were further characterized by Raman and photoluminescence (PL) spectroscopy. Exemplary spectra of Raman and PL characterization are shown in Fig. 1c and Fig 1d. In the Raman spectrum, the E^1_{2g} and A_{1g} modes can be clearly identified. The difference in their positions is about 21 /cm, in agreement with the value expected for monolayers. In the PL spectrum, a strong peak at 1.84 eV and a smaller peak at around 1.98 eV, corresponding to the A and B exciton in single-layer MoS_2, are observed [17,18]. Both results confirm monolayered MoS_2 [3,45]. We note that small peak position variations in Raman as well as in PL spectra can occur because of the CVD growth process resulting in slightly strained MoS_2 flakes [46–48].

Selected flakes were contacted by metal leads of Ni (3.5 nm) and Au (75 nm), used as adhesion and cover layers, respectively. Ni was selected to achieve ohmic contacts [49] and was deposited by electron beam evaporation at a rate of 0.01 nm per second in high vacuum (10^{-6} mbar) to reduce the contact resistance [50–52].

The devices like the ones displayed in the optical image of Fig. 1e are made of one or more flakes between each couple of leads. The MoS_2 flakes constitute the channel, whereas the Ni/Au leads are the source (S) and drain (D), and the Si substrate is the common back-gate of the FETs (Fig. 1f). Although several transistors were fabricated and studied, showing similar behavior, in the following most of the electrical characterization refers to the transistor between the leftmost leads, labeled as S and D in Fig. 1e and Fig. 1f, connected by a monolayer triangular flake forming a trapezoidal channel of length L = 4.1 μm and width W decreasing from W_1 = 15.6 μm (S) to W_2 = 5.6 μm (D) resulting in an area of Σ = 43.5 μm^2.

2.2. Conductivity in dark

Fig. 2a and Fig. 2b show the transistor characterization in terms of the output characteristics (drain current *vs.* drain voltage , $I_d - V_{ds}$, for different gate voltages V_{gs}) and the transfer characteristics ($I_d - V_{gs}$ for

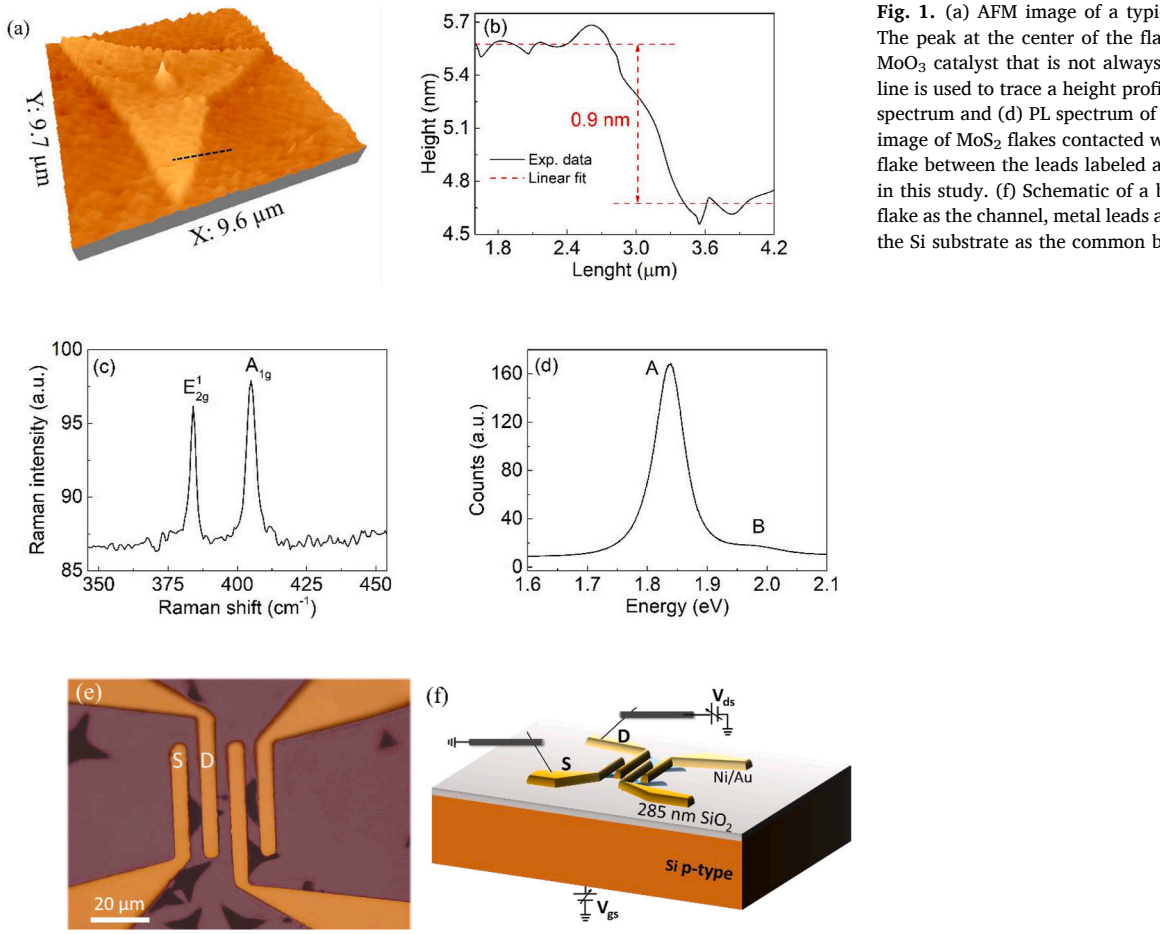

Fig. 1. (a) AFM image of a typical monolayer MoS_2 flake. The peak at the center of the flake corresponds to residual MoO_3 catalyst that is not always present. The black dotted line is used to trace a height profile shown in (b). (c) Raman spectrum and (d) PL spectrum of the MoS_2 flake. (e) Optical image of MoS_2 flakes contacted with Ni/Au leads. The MoS_2 flake between the leads labeled as S and D was mostly used in this study. (f) Schematic of a back-gate FET with a MoS_2 flake as the channel, metal leads as the source and drain, and the Si substrate as the common back-gate.

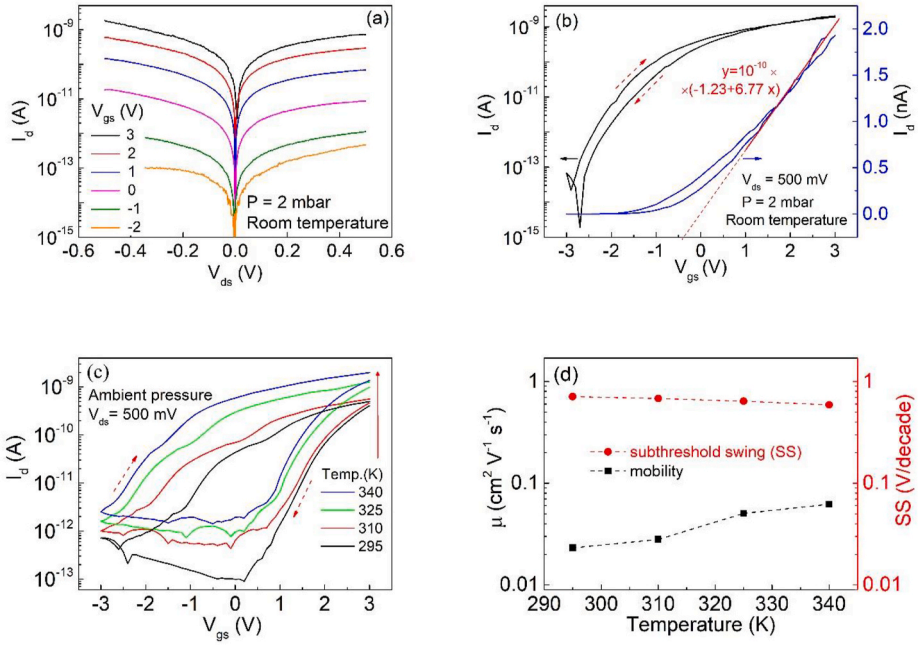

Fig. 2. (a) Output characteristics for different V_{gs}. (b) Transfer characteristics at V_{ds} = 500 mV and pressure of 2 mbar for a forward and a reverse V_{gs} sweep, on logarithmic (black) and linear (blue) scale. (c) Transfer characteristics at V_{ds} = 500 mV, ambient pressure, and for different temperatures. (d) Mobility (black) and subthreshold swing SS (red) as a function of temperature. All measurements are performed in dark.

fixed V_{ds}) in dark, at room temperature and pressure of 2 mbar. The output characteristics show near-ohmic behavior with a slight asymmetry in the current, pointing to low Schottky barrier contacts [53,54]. The decreasing current for negative V_{gs} is typical of an n-type device. Owing to the formation of interfacial metal sulfides, facilitated by the presence of defects, Ni constitutes covalent contacts with MoS_2 that cause Fermi level alignment in the upper part of the MoS_2 bandgap [49,50,55]. Such a band alignment favors the injection of electrons in the channel. The transfer characteristic confirms that the device is a normally on n-type transistor with a modulation of five orders of magnitude over the narrow $V_{gs} = \pm 3$ V range, corresponding to a subthreshold swing $SS = \frac{dV_{ds}}{d(\log(I_d))} = 0.6$ V/decade. The high current at $V_{gs} = 0$ V indicates a high intrinsic doping of MoS_2, which is usually attributed to S vacancies as sulfur-deficient MoS_2 has n-type behavior [4–8].

Using the fit of the linear part of the transfer characteristic on a linear scale, as shown in Fig. 2b (right), and considering the trapezoidal shape of the flake, the mobility is estimated as $\mu = \frac{1}{C_{ox}} \frac{L}{W_1 - W_2} \ln\left(\frac{W_1}{W_2}\right) \left(\frac{1}{V_{ds}}\right) \left(\frac{dI_d}{dV_{gs}}\right) = 0.05$ cm^2/V/s ($C_{ox} = 12.11$ nF/cm^2 is the oxide capacitance per unit area). Likewise, a threshold voltage $V_{th} \approx -0.4$ V can be estimated. The low mobility is consistent with results reported for similar devices and is caused by process residuals, surface roughness, interfacial traps, and intrinsic defects (the most common defect type in such CVD grown flakes is a sulfur vacancy with a typical defect density on the order of 10^{13}/cm^2) [56,57], with limited contribution of adsorbates as the measurements are performed at a low pressure of 2 mbar [58–62].

The transfer characteristics of Fig. 2b exhibit a clockwise narrow hysteresis, which is significantly enhanced when the device is exposed to air, as shown in Fig. 2c. Hysteresis is caused by charge capture and emission processes involving MoS_2/SiO_2 interface states and fabrication residues [63–65]; moreover, the clockwise behavior at room temperature indicates an important effect of MoS_2 intrinsic defects [63], consistently with the measured low mobility. The dramatic enhancement of hysteresis upon exposure to air (Fig. 2c) indicates a dominant effect of adsorbates, such as O_2 and H_2O molecules, whose adsorption is favored (disfavored) at positive (negative) gate voltage [30,66–68]. Fig. 2c shows that the form of the transfer curves remains unaltered when the temperature is increased, although both the on and off currents increase. It can also be observed that the SS, evaluated using the reverse sweep, remains constant over the (295–340) K temperature range, while the mobility increases slightly (see Fig. 2d), pointing to a thermally activated hopping transport mechanism with Coulomb scattering from charged impurities as the main scattering mechanism [69–71].

2.3. Photoconductivity

Fig. 3a and Fig. 3b shows the output and transfer characteristics of the transistor at room temperature and a pressure of 2 mbar, in dark and under illumination by an array of white LEDs producing a light of intensity $I = 1.75$ mW/cm^2 on the device. It can be observed that the current increases up to 6 orders of magnitude at negative V_{gs}, confirming the high photoconductivity of MoS_2 [25,38,72]. Under illumination, the transistor does not switch off, and only a small current modulation is observed over the $V_{gs} = \pm 3$ V range. This means that under light the transistor undergoes a photogating effect that manifests as a significant decrease in the threshold voltage and the left shift of the transfer characteristic with consequent increase of the current [26]. The photogating effect has been primarily attributed to charge trapping at the MoS_2/SiO_2 interface and to molecules adsorbed on the channel, which give rise to a slow photoresponse [26,29].

The photocurrent $I_{ph} = |I_{light}| - |I_{dark}|$, where I_{light} and I_{dark} are the currents under illumination and in dark, respectively, is shown in Fig. 3b (dashed blue lines). It can be observed that the maximum photocurrent is achieved at $V_{gs} = 3$ V. In such condition, the responsivity is $R = \frac{I_{ph}}{P_{in}} \approx 30$ A/W ($P_{in} = I\Sigma$ is the power incident on the device). We note that the responsivity is consistent with or higher than the responsivities that have been reported for similar MoS_2 devices [72–75].

Fig. 3c shows the time-resolved photocurrent I_{ph} under illumination by a laser at different wavelengths, for 240 s long pulses. The measurements were performed at room temperature and in air with the grounded gate, that is, above threshold. Indeed, the photocurrent pulses can be fitted by a double exponential growth/decay, $I_{ph} = I_0 + a_1 \exp\left(-\frac{t-t_0}{\tau_1}\right) + a_2 \exp\left(-\frac{t-t_0}{\tau_2}\right)$, with time constants $\tau_1 \sim 10$ s (slow response) and

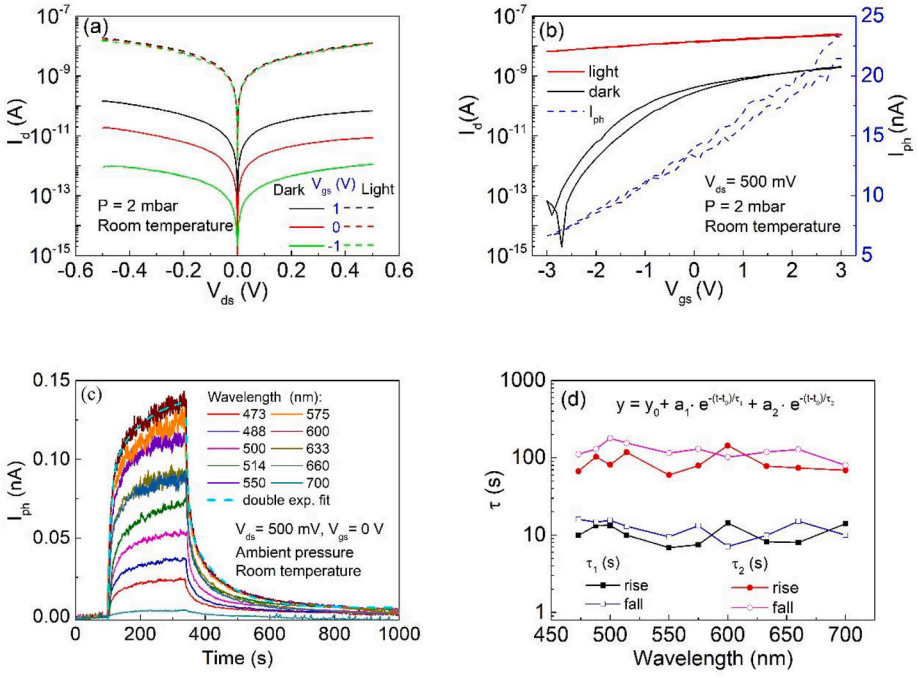

Fig. 3. (a) Output characteristics in dark (solid curves) and light (dashed curves) for $V_{gs} = 0, \pm 1$ V. (b) Transfer characteristics at $V_{ds} = 500$ mV for forward and reverse V_{gs} sweeps on logarithmic scale in dark (black) and light (red). The blue dashed line is the photocurrent I_{ph}. (c) Time-resolved photocurrent as a function of wavelength, from 450 nm to 700 nm and 20 nm bandwidth (the cyan dashed line represents a typical double rise/decay fit). (d) Rise and fall time constants of the pulses of Figure (c) fitted by a double exponential growth/decay.

$\tau_2 \sim 100$ s (slower response), respectively (Fig. 3d).

Three main mechanisms contribute to the photoresponse, namely the ultrafast electron–hole direct photogeneration, a slow-response photobolometric effect in which electrons are detrapped from shallow in-gap states [40], and a slower-response photogating effect dominated by desorption of polar adsorbates and detrapping of electrons from deep donor-like in-gap states that get positively charged [76]. These mechanisms are summarized in Fig. 4a and Fig. 4b.

The double exponential fit with long τ_1 and τ_2 time constants indicates that photobolometric and photogating effects with slow and slower response, respectively, are the dominant mechanisms in time-resolved photoresponse [76]. We remark that similar τ_1 and τ_2 time constants have been reported before and have been consistently attributed to trap states in the bandgap caused by sulfur vacancies and adsorption of oxygen, respectively [24,28,42]. The time constants of the optical direct transitions, which should result in a photoresponse with characteristic times below the ns regime [23,77], are not resolved in our measurements limited by a sampling rate of few Hz.

The shorter time constant τ_1 can be attributed to photobolometric electron detrapping (Fig. 4b) from shallow intragap states caused by sulfur vacancies and other defects or impurities [78], that can be significantly slower than the direct electron–hole pair photogeneration [38]. As these defects are inadvertently introduced during the fabrication process, this time constant can depend on the synthesis method and can vary from device to device.

The maximum photocurrent, $I_{ph,max}$, extracted from the data of Fig. 3c by averaging the photocurrent in the time interval 320–340s, that is, at the end of the light pulse, as a function of the wavelength shows a peak with a maximum at 571 nm (Fig. 4c), corresponding to 2.17 eV, an energy higher than the A and B optical absorption peaks of monolayer MoS_2 (as shown in Fig. 1d). A blue shift of the optical bandgap, around 50 meV, can be caused by tensile strain, for instance, induced by either the CVD process or the metal contacts [79–81]. However, this is small to account for the observed blue shift. Therefore, the observed photocurrent cannot be easily explained by direct band-to-band transitions. Besides, the short lifetime of photogenerated carriers and the measured low mobility do not favor the direct collection of photogenerated electron–hole pairs at the metal leads. Remarkably, the measured photoconductivity peak is in the 1.9–2.4 eV range of physio-adsorption energy of O_2 and H_2O on defective MoS_2 as estimated by DFT calculations (we note that the adsorption energy of O_2 on perfect MoS_2 is much lower, ~-10 meV) [32,82–84]. Moreover, numerical calculations have indicated that the optical absorbance of MoS_2 is affected by the physisorption of the O_2 and H_2O molecules on both defective and pristine surfaces [85,86]. These facts, combined with the measured long rise and decay times, lead to the conclusion that the long-time evolution of the photocurrent can be dominated by light-induced desorption of adsorbates.

As depicted in Fig. 4a, when O_2 and H_2O molecules are physisorbed on the MoS_2 surface, electrons are transferred from MoS_2, producing a p-doping effect, that is, a decrease in the MoS_2 conductivity [31,85,87]. The electron transfer occurs from Mo 4d orbitals to the 2p orbitals of the O_2, with a reaction like $e^- + O_2 \rightarrow O_2^-$. The strong Coulomb attraction between O_2^- and Mo^{4+} ions can result in the chemical adsorption bond, especially on defective sites. As shown in Fig. 4a and Fig. 4b, light induces interband transitions and excites electrons from the 2p orbitals of the O_2^- back to the Mo 4d orbitals ($O_2^- \rightarrow O_2 + e^-$). The temporarily neutralized O_2 molecules can easily desorb from the MoS_2 surface, thus causing an increase in the electron density and the conductivity of the MoS_2 layer. The photoexcitation and photodesorption processes are inevitably accompanied by the recombination and re-adsorption; therefore, they require a long illumination time to yield a current rise, thus justifying the longer τ_2 time constant.

The above-described mechanism applies also to physisorbed water. A laser irradiation can sweep away the H_2O adsorbed on the MoS_2 surface resulting in enhanced conductivity.

Defects largely impact the adsorption rate of O_2, H_2O and other molecules. The density of defects, obviously desired as low as possible, is rather uncontrollable unless the defects are intentionally introduced. This uncontrollability introduces large fluctuations in the distribution of the above-mentioned longer τ_2 time constant.

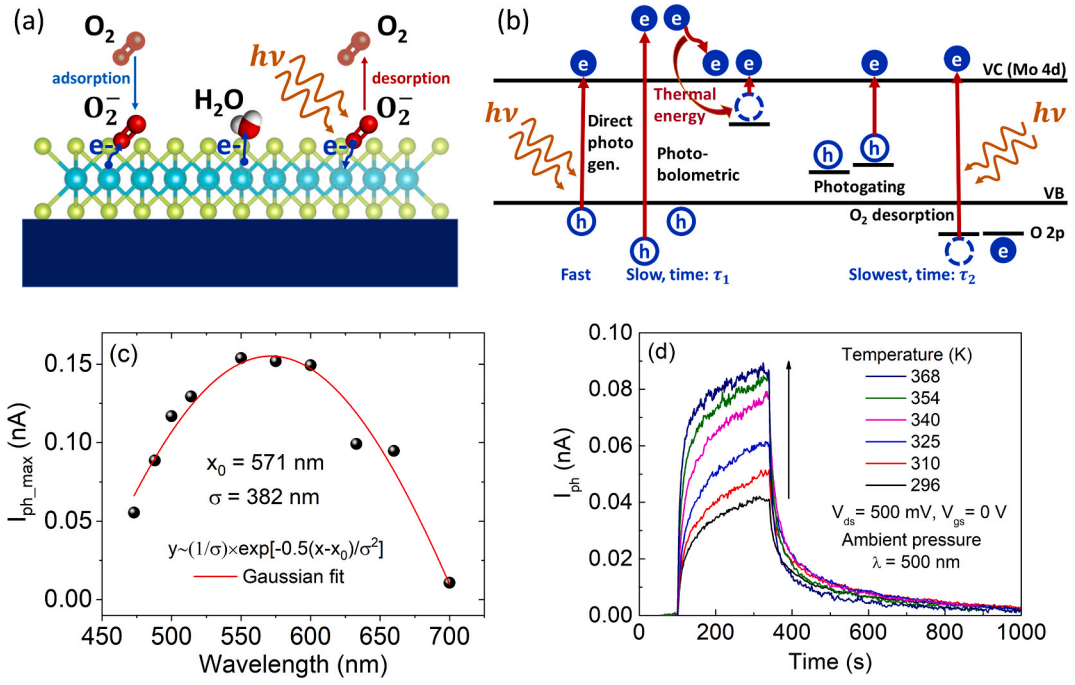

Fig. 4. (a) Adsorption and desorption of O_2 and H_2O with charge transfer mechanisms. (b) Band diagram showing the main mechanisms involved in the MoS_2 photoresponse: direct electron–hole photogeneration, photobolometric effect, photogating effect, detrapping of electrons, and desorption of O_2 molecules. (c) Maximum photocurrent as a function of wavelength with Gaussian fit (red line). (d) Time-resolved photocurrent as a function of temperature for light pulses of fixed intensity and duration, as well as 500 nm wavelength.

Obviously, the impact of adsorbates on the rise and decay time constants can be minimized in devices with passivated or incapsulated MoS_2, for instance, with methylamine halide [88] or hexagonal boron nitride [76], where a fast photoresponse has been reported.

2.4. Photoconductivity vs temperature

We investigated the photocurrent at different temperatures, from room temperature to 370 K, with the device in air exposed to light pulses of fixed power/duration and 500 nm wavelength. Fig. 4d shows that the photocurrent increases with the temperature. We point out that the effect of temperature on the dark current I_{dark} is not included in the plot as only the photocurrent I_{ph} is displayed. To gain more insight, we checked the behavior of the photocurrent with light at $\lambda = 600$ nm, that is, at a wavelength closer to the maximum photoresponse. Fig. 5a confirms that the photocurrent depends on temperature and is enhanced at higher temperatures. The phenomenon is reversible as the photocurrent decreases with the decreasing temperature, as shown in Fig. 5b. The maximum photocurrent, taken around the end of the light pulse, is displayed in Fig. 5c for both increasing and decreasing temperature and shows that the photocurrent is not characterized by any obvious hysteresis over a temperature loop.

The comparison of the temperature behavior of the dark current and the maximum photocurrent (see slopes in Fig. 5d) shows that the photocurrent, especially at $\lambda = 600$ nm, is much more sensitive to temperature than the dark current.

The dark current increases with temperature because of thermal generation or excitation of charge carries from trap states, or simply due to the enhanced carrier injection from the contacts [89]. The very low slope of I_{dark} as shown in Fig. 5d demonstrates that these processes are marginally increased by temperature in the 290–370 K range. Conversely, the maximum photocurrent shows a linear increase with temperature, that is, significantly higher, by more than a factor of 10, when the light has energy close to the MoS_2 bandgap and O_2/H_2O adsorption energy.

The enhancement of the photocurrent with temperature can be explained by a combined effect of the thermal and optical energies that contribute to the detrapping of carriers and desorption of adsorbates. At a given photoexcitation, more O_2 and H_2O molecules desorb from the surface of the MoS_2 as the temperature increases; hence, more electrons are available for conduction.

The temperature-dependent photoinduced adsorbate desorption should be facilitated by the decreasing pressure. Hence, the enhancement of photocurrent by temperature is expected to be more pronounced at low pressure. This is confirmed by the measurements as shown in Fig. 6 that reports the time-resolved photocurrent vs temperature at low pressure, namely 10^{-5} and 2 mbar.

While the temperature-enhanced photoconductivity is confirmed in vacuum, it can be observed that under white laser pulses of fixed power/duration the photocurrent is higher at 10^{-5} mbar than at 2 mbar (Fig. 6a and Fig. 6b). This confirms that the lower pressure facilitates the light/temperature-induced desorption process. Moreover, there is a different long-time photocurrent dynamics as a persistent photoconductivity is observed at low pressure [25,27,90,91]. In vacuum, desorbed adsorbates are removed from the chamber, which make the re-adsorption process very slow and prevent the current returning to the initial state. Indeed, the inset of Fig. 6a and Fig. b show a gradual increase of the dark current for repeated light pulses because very long times are needed to achieve the pristine state. Fig. 6c compares the currents at three different pressures (ambient, 2 mbar, and 10^{-5} mbar) and summarizes the key aspects of the process: at a given temperature, the photoinduced desorption of adsorbates is more effective at lower pressure, resulting in a higher photocurrent; likewise, the photocurrent decay is slower at lower pressure because the reverse process of re-adsorption is suppressed. Again, the transient photocurrent at low pressure is well fitted by a double exponential decay. Fig. 6d highlights

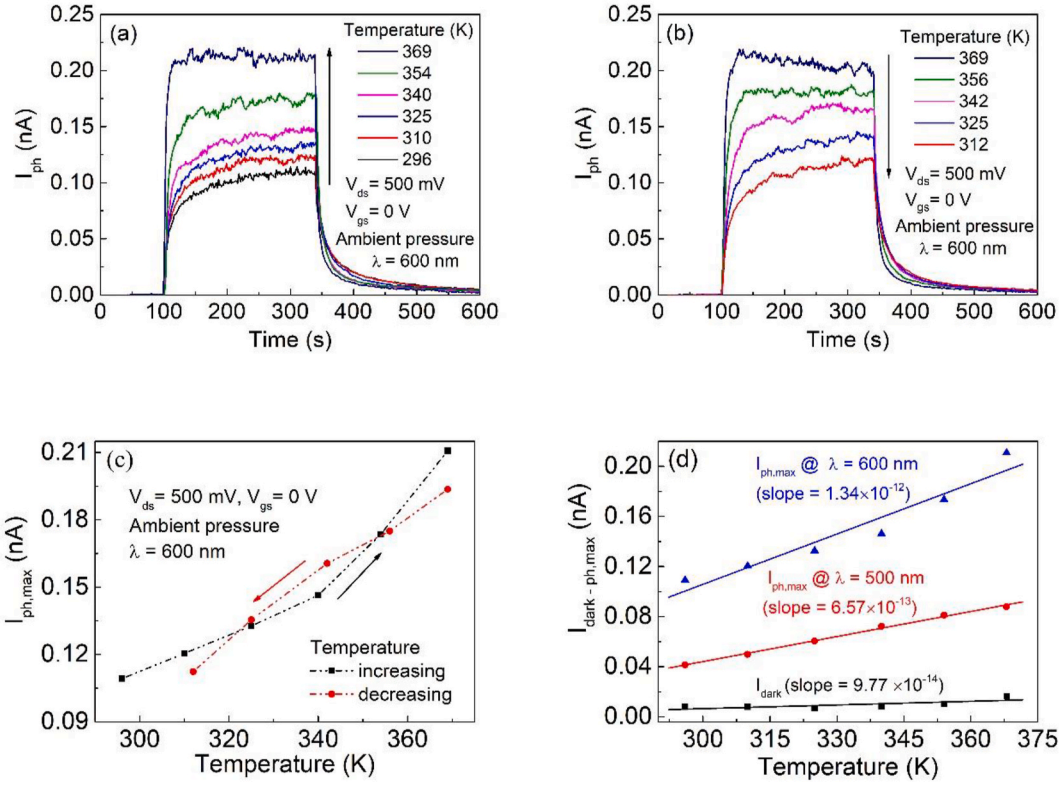

Fig. 5. Time-resolved photocurrent at 600 nm wavelength for (a) increasing and (b) decreasing temperature. (c) Maximum photocurrent at 600 nm for increasing (black) and decreasing (red) temperature. (d) Maximum photocurrent as a function of temperature in dark (black) and under 500 nm (red) and 600 nm (blue) light.

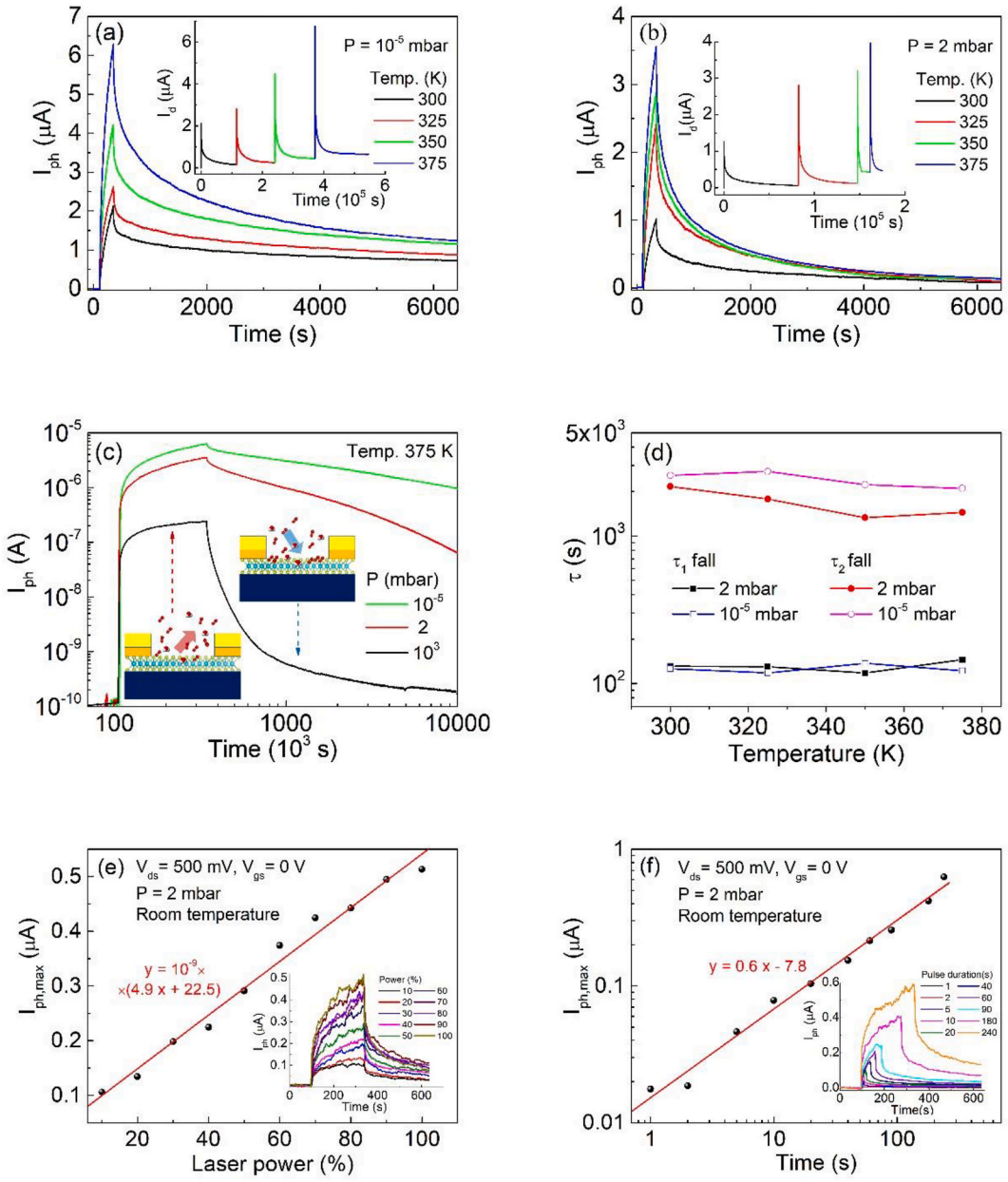

Fig. 6. Time-resolved photocurrent under white light pulses of fixed power (2 mW) and duration, at different temperatures and pressure (a) 10^{-5} mbar and (b) 2 mbar. The insets in (a) and (b) show the current vs. time for consecutive light pulses. (c) Time-resolved photocurrent at different pressures and 375 K temperature. The cartoons show adsorption (top) and desorption (bottom) of molecules from the MoS_2 surface. (d) Time constants τ_1 and τ_2 from a double rise/decay exponential fit of the photocurrent at 10^{-5} mbar (Figure a) and 2 mbar (Figure b). (e) Maximum photocurrent as a function of the white light power (as a fraction of the maximum laser power) for pulses of fixed duration. (f) Maximum photocurrent as a function of the exposure time for a given white light power. The insets in (e) and (f) show the time-resolved photocurrent.

that in vacuum the decay times are extended because the re-adsorption process is strongly suppressed.

Finally, turning our attention to practical applications, a sensitive photodetector, which can also distinguish different light intensities, is highly desirable. To demonstrate this, Fig. 6e shows that for the device under study, the maximum photocurrent is a linear function of the laser power. Moreover, as shown in Fig. 6f, the photocurrent is a power law function, with an exponent of 0.6, of the light exposure time, enabling the control of the exposure time. The power law behavior is typical of gas sensors and can be explained by the heterogeneous (Freundlich) adsorption, further confirming the key role of adsorbates in the MoS_2 photoresponse [92–94].

The power and exposure time dependence of the photocurrent confirms that monolayer MoS_2 can be used in photodetectors with extended functionalities.

3. Conclusions

Back-gate monolayer MoS_2 transistors with Ni/Au contacts have been fabricated and characterized. Their photoconductivity has been studied as a function of temperature and pressure. It has been shown that the time-resolved photocurrent behavior is dominated by slow photobolometric and slower photogating effects that are attributed to charge trapping/detrapping by shallow and deeper intragap states as well as to desorption of polar adsorbates. Above room temperature, the photocurrent is enhanced by increasing temperature and decreasing pressure. The temperature dependence of photoconductivity can be explained by photoinduced desorption of adsorbates, such as O_2 and

H_2O molecules, that enhance the n-doping level of the MoS_2 channel. Such a process is facilitated at low pressure, which also suppresses the re-adsorption mechanisms, thus yielding a persistent photocurrent.

This study has clarified how intrinsic defects and adsorbates on the MoS_2 surface play a key role in the temperature behavior of the time-resolved photoresponse of the material. The conclusions can be easily extended to other 2D materials.

4. Experimental section/methods

MoS_2 flakes were grown via CVD over a highly doped p-type Si substrate (resistivity 0.001–0.005 Ω cm) covered by 285 nm thermal SiO_2 that was spin coated with a 1% sodium cholate solution. The growth was performed in a three-zone split tube furnace. The O_2 content of the furnace was minimized via a 15 min purging process with 1000 N cm^3/min Ar gas flow. A total of 50 mg of S powder were positioned in the upstream heating zone at 150 °C. MoO_3, which is used as the source for molybdenum, was obtained from a saturated ammonium heptamolybdate (AHM) solution initially annealed at 300 °C under ambient conditions and placed in the next downstream zone at 800 °C. During the process, 500 N cm^3/min of Ar gas was flown through the quartz tube. The growth process lasted 15 min and was followed by a rapid cooling. At a temperature of around 100 °C, the samples were retrieved from the oven. The resulting MoS_2 triangular or star-shaped flakes are typically monolayers (in some areas also few-layer MoS_2 grows) of the 2H phase, as shown by the respective Raman spectra (see Fig. 1a) and HR-STEM measurements [95].

The AFM image of MoS_2 flake, see Fig. 1a, was acquired by using a Nanosurf A.G. microscope. The Raman and PL measurements were performed with a WITec alpha300 RA confocal Raman spectrometer. All measurements were performed with an excitation wavelength of 532 nm and with an output power of 0.5 mW. Grid sizes were switched between 300 g/mm for PL spectra and 1800 g/mm for Raman spectra measurements (see Fig. 1c and Fig. 1d). For the device fabrication, the Ni was used for the metal contacts. The metal's patterning was carried out through standard photolithography and lift-off processes (see Fig. 1e and Fig. 1f).

The electrical measurements were performed using a cryogenic probe station with pressure control down to 10^{-5} mbar and endowed with four metallic nanoprobes, connected to a Keithley 4200 semiconductor characterization system (Tektronix Inc.). The photoresponse was investigated under the illumination by an array of white LEDs or by a supercontinuum white laser (SuperK COMPACT by NKT Photonics) with a maximum power of 110 mW, wavelength in the range 450–2400 nm, and 1 mm beam diameter. Light at a given wavelengths was selected using a monochromator (Sciencetech Inc.) with 20 nm bandwidth.

Credit author statement

Antonio Di Bartolomeo: conceptualization, methodology, data curation, writing- original draft preparation, supervision. **Arun Kumar**: methodology, software, investigation. **Ofelia Durante**: software, investigation, visualization. **Andrea Sessa**: software, investigation, visualization. **Enver Faella**: data curation, investigation, validation. **Loredana Viscardi**: data curation, investigation, validation. **Kimberly Intonti**: data curation, investigation, validation. **Filippo Giubileo**: methodology, data curation, investigation, validation. **Nadia Martucciello**: methodology, data curation, investigation, validation. **Paola Romano**: software, data curation, visualization. **Stephan Sleziona**: methodology, writing- reviewing and editing, investigation, validation. **Marika Schleberger**: conceptualization, methodology, writing-reviewing and editing, validation.

Funding sources

A.D.B. and A.K. acknowledge the financial support from the European Union's REACT-EU PON Research and Innovation 2014–2020, Ministerial Decree 1062/2021, and from the University of Salerno, with grant ORSA223384. M.S. and S.S. acknowledge financial support from the DFG within the SFB 1242 ('Non-Equilibrium Dynamics of Condensed Matter in the Time Domain') project C5, #278162697 and by project INST-429784087. S.S. thanks the ERASMUS+ program for financial support.

Declaration of competing interest

The authors declare that they have no known competing financial interests or personal relationships that could have appeared to influence the work reported in this paper.

Data availability

Data will be made available on request.

References

[1] V.P. Kumar, D.K. Panda, Review – next generation 2D material molybdenum disulfide (MoS_2): properties, applications and challenges, ECS J. Solid State Sci. Technol. 11 (3) (2022), 033012, https://doi.org/10.1149/2162-8777/ac5a6f.
[2] D. Gupta, V. Chauhan, R. Kumar, A comprehensive review on synthesis and applications of molybdenum disulfide (MoS2) material: past and recent developments, Inorg. Chem. Commun. 121 (2020), 108200, https://doi.org/10.1016/j.inoche.2020.108200.
[3] K.F. Mak, C. Lee, J. Hone, J. Shan, T.F. Heinz, Atomically thin MoS2: a new direct-gap semiconductor, Phys. Rev. Lett. 105 (13) (2010), 136805, https://doi.org/10.1103/PhysRevLett.105.136805.
[4] S. McDonnell, R. Addou, C. Buie, R.M. Wallace, C.L. Hinkle, Defect-dominated doping and contact resistance in MoS_2, ACS Nano 8 (3) (2014) 2880–2888, https://doi.org/10.1021/nn500044q.
[5] J. Pető, T. Ollár, P. Vancsó, Z.I. Popov, G.Z. Magda, G. Dobrik, C. Hwang, P. B. Sorokin, L. Tapasztó, Spontaneous doping of the basal plane of MoS2 single layers through oxygen substitution under ambient conditions, Nat. Chem. 10 (12) (2018) 1246–1251, https://doi.org/10.1038/s41557-018-0136-2.
[6] J. Yang, F. Bussolotti, H. Kawai, K.E.J. Goh, Tuning the conductivity type in monolayer WS_2 and MoS_2 by sulfur vacancies, Phys. Rapid Res. Lett. 14 (9) (2020), 2000248, https://doi.org/10.1002/pssr.202000248.
[7] C. Marquez, N. Salazar, F. Gity, J.C. Galdon, C. Navarro, C. Sampedro, P.K. Hurley, E.Y. Chang, F. Gamiz, Hysteresis in As-synthesized MoS2 transistors: origin and sensing perspectives, Micromachines 12 (6) (2021) 646, https://doi.org/10.3390/mi12060646.
[8] J. Suh, T.-E. Park, D.-Y. Lin, D. Fu, J. Park, H.J. Jung, Y. Chen, C. Ko, C. Jang, Y. Sun, R. Sinclair, J. Chang, S. Tongay, J. Wu, Doping against the native propensity of MoS_2: degenerate hole doping by cation substitution, Nano Lett. 14 (12) (2014) 6976–6982, https://doi.org/10.1021/nl503251h.
[9] T. Pham, G. Li, E. Bekyarova, M.E. Itkis, A. Mulchandani, MoS_2-based optoelectronic gas sensor with sub-parts-per-billion limit of NO_2 gas detection, ACS Nano 13 (3) (2019) 3196–3205, https://doi.org/10.1021/acsnano.8b08778.
[10] D. Burman, H. Raha, B. Manna, P. Pramanik, P.K. Guha, Substitutional doping of MoS_2 for superior gas-sensing applications: a proof of concept, ACS Sens. 6 (9) (2021) 3398–3408, https://doi.org/10.1021/acssensors.1c01258.
[11] S. Tajik, Z. Dourandish, F. Garkani Nejad, H. Beitollahi, P.M. Jahani, A. Di Bartolomeo, Transition metal dichalcogenides: synthesis and use in the development of electrochemical sensors and biosensors, Biosens. Bioelectron. 216 (2022), 114674, https://doi.org/10.1016/j.bios.2022.114674.
[12] W. Zhang, P. Zhang, Z. Su, G. Wei, Synthesis and sensor applications of MoS_2-based nanocomposites, Nanoscale 7 (44) (2015) 18364–18378, https://doi.org/10.1039/C5NR06121K.
[13] B. Radisavljevic, A. Radenovic, J. Brivio, V. Giacometti, A. Kis, Single-layer MoS2 transistors, Nat. Nanotechnol. 6 (3) (2011) 147–150, https://doi.org/10.1038/nnano.2010.279.
[14] M. Saeed, W. Uddin, A.S. Saleemi, M. Hafeez, M. Kamil, I.A. Mir, Sunila, R. Ullah, S.U. Rehman, Z. Ling, Optoelectronic properties of MoS2-ReS2 and ReS2-MoS2 heterostructures, Phys. B Condens. Matter 577 (2020), 411809, https://doi.org/10.1016/j.physb.2019.411809.
[15] M. Bernardi, M. Palummo, J.C. Grossman, Extraordinary sunlight absorption and one nanometer thick photovoltaics using two-dimensional monolayer materials, Nano Lett. 13 (8) (2013) 3664–3670, https://doi.org/10.1021/nl401544y.
[16] J.Y. Kwak, Absorption coefficient estimation of thin MoS2 film using attenuation of silicon substrate Raman signal, Results Phys. 13 (2019), 102202, https://doi.org/10.1016/j.rinp.2019.102202.
[17] R. Ganatra, Q. Zhang, Few-layer MoS_2: a promising layered semiconductor, ACS Nano 8 (5) (2014) 4074–4099, https://doi.org/10.1021/nn405938z.
[18] C. Qin, Y. Gao, Z. Qiao, L. Xiao, S. Jia, Atomic-layered MoS_2 as a tunable optical platform, Adv. Opt. Mater. 4 (10) (2016) 1429–1456, https://doi.org/10.1002/adom.201600323.

[19] M. Bernardi, C. Ataca, M. Palummo, J.C. Grossman, Optical and electronic properties of two-dimensional layered materials, Nanophotonics 6 (2) (2017) 479–493, https://doi.org/10.1515/nanoph-2015-0030.

[20] Q. Peng, S. De, Outstanding mechanical properties of monolayer MoS2 and its application in elastic energy storage, Phys. Chem. Chem. Phys. 15 (44) (2013), 19427, https://doi.org/10.1039/c3cp52879k.

[21] H.S. Nalwa, A review of molybdenum disulfide (MoS_2) based photodetectors: from ultra-broadband, self-powered to flexible devices, RSC Adv. 10 (51) (2020) 30529–30602, https://doi.org/10.1039/D0RA03183F.

[22] A. Taffelli, S. Dirè, A. Quaranta, L. Pancheri, MoS2 based photodetectors: a review, Sensors 21 (8) (2021) 2758, https://doi.org/10.3390/s21082758.

[23] H. Wang, C. Zhang, W. Chan, S. Tiwari, F. Rana, Ultrafast response of monolayer molybdenum disulfide photodetectors, Nat. Commun. 6 (1) (2015) 8831, https://doi.org/10.1038/ncomms9831.

[24] M.F. Khan, M.W. Iqbal, M.Z. Iqbal, M.A. Shehzad, Y. Seo, J. Eom, Photocurrent response of MoS_2 field-effect transistor by deep ultraviolet light in atmospheric and N_2 gas environments, ACS Appl. Mater. Interfaces 6 (23) (2014) 21645–21651, https://doi.org/10.1021/am506716a.

[25] A. George, M.V. Fistul, M. Gruenewald, D. Kaiser, T. Lehnert, R. Mupparapu, C. Neumann, U. Hübner, M. Schaal, N. Masurkar, L.M.R. Arava, I. Staude, U. Kaiser, T. Fritz, A. Turchanin, Giant persistent photoconductivity in monolayer MoS2 field-effect transistors, NPJ 2D Mater. Appl. 5 (1) (2021) 15, https://doi.org/10.1038/s41699-020-00182-0.

[26] A. Di Bartolomeo, L. Genovese, T. Foller, F. Giubileo, G. Luongo, L. Croin, S.-J. Liang, L.K. Ang, M. Schleberger, Electrical transport and persistent photoconductivity in monolayer MoS_2 phototransistors, Nanotechnology 28 (21) (2017), 214002, https://doi.org/10.1088/1361-6528/aa6d98.

[27] Chandan, S. Sarkar, B. Angadi, Defects induced persistent photoconductivity in monolayer MoS_2, Appl. Phys. Lett. 118 (17) (2021), 172105, https://doi.org/10.1063/5.0048505.

[28] K. Czerniak-Łosiewicz, M. Świniarski, A.P. Gertych, M. Giza, Z. Maj, M. Rogala, P. J. Kowalczyk, M. Zdrojek, Unraveling the mechanism of the 150-fold photocurrent enhancement in plasma-treated 2D TMDs, ACS Appl. Mater. Interfaces 14 (29) (2022) 33984–33992, https://doi.org/10.1021/acsami.2c06578.

[29] P. Han, E.R. Adler, Y. Liu, L. St Marie, A. El Fatimy, S. Melis, E. Van Keuren, P. Barbara, Ambient effects on photogating in MoS_2 photodetectors, Nanotechnology 30 (28) (2019), 284004, https://doi.org/10.1088/1361-6528/ab149e.

[30] A. Di Bartolomeo, L. Genovese, F. Giubileo, L. Iemmo, G. Luongo, T. Foller, M. Schleberger, Hysteresis in the transfer characteristics of MoS_2 transistors, 2D Mater 5 (1) (2017), 015014, https://doi.org/10.1088/2053-1583/aa91a7.

[31] C. Hou, J. Deng, J. Guan, Q. Yang, Z. Yu, Y. Lu, Z. Xu, Z. Yao, J. Zheng, Photoluminescence of monolayer MoS_2 modulated by water/O_2/laser irradiation, Phys. Chem. Chem. Phys. 23 (43) (2021) 24579–24588, https://doi.org/10.1039/D1CP03651C.

[32] R. Wang, X. Wang, Z. Zuo, S. Ni, J. Dai, D. Wang, Adsorption equilibrium and mechanism and of water molecule on the surfaces of molybdenite (MoS2) based on kinetic Monte-Carlo method, Molecules 27 (24) (2022) 8710, https://doi.org/10.3390/molecules27248710.

[33] Z. Peng, R. Yang, M.A. Kim, L. Li, H. Liu, Influence of O_2, H_2O and airborne hydrocarbons on the properties of selected 2D materials, RSC Adv. 7 (43) (2017) 27048–27057, https://doi.org/10.1039/C7RA02130E.

[34] E. Faella, K. Intonti, L. Viscardi, F. Giubileo, A. Kumar, H.T. Lam, K. Anastasiou, M. F. Craciun, S. Russo, A. Di Bartolomeo, Electric transport in few-layer ReSe2 transistors modulated by air pressure and light, Nanomaterials 12 (11) (2022) 1886, https://doi.org/10.3390/nano12111886.

[35] B. Cui, Y. Xing, J. Han, W. Lv, W. Lv, T. Lei, Y. Zhang, H. Ma, Z. Zeng, B. Zhang, Negative photoconductivity in low-dimensional materials, Chin. Phys. B 30 (2) (2021), 028507, https://doi.org/10.1088/1674-1056/abcf41.

[36] A. Grillo, E. Faella, A. Pelella, F. Giubileo, L. Ansari, F. Gity, P.K. Hurley, N. McEvoy, A. Di Bartolomeo, Coexistence of negative and positive photoconductivity in few-layer PtSe2 field-effect transistors, arXiv:2107.09492 [cond-mat] (2021), https://doi.org/10.1002/adfm.202105722.

[37] F. Urban, F. Gity, P.K. Hurley, N. McEvoy, A. Di Bartolomeo, Isotropic conduction and negative photoconduction in ultrathin $PtSe_2$ films, Appl. Phys. Lett. 117 (19) (2020), 193102, https://doi.org/10.1063/5.0021009.

[38] M.M. Furchi, D.K. Polyushkin, A. Pospischil, T. Mueller, Mechanisms of photoconductivity in atomically thin MoS_2, Nano Lett. 14 (11) (2014) 6165–6170, https://doi.org/10.1021/nl502339q.

[39] M. Buscema, J.O. Island, D.J. Groenendijk, S.I. Blanter, G.A. Steele, H.S.J. van der Zant, A. Castellanos-Gomez, Photocurrent generation with two-dimensional van Der Waals semiconductors, Chem. Soc. Rev. 44 (11) (2015) 3691–3718, https://doi.org/10.1039/C5CS00106D.

[40] V.K. Pulikodan, A. Alexander, A.B. Pillai, M.A.G. Namboothiry, Photoresponse of solution-processed molybdenum disulfide nanosheet-based photodetectors, ACS Appl. Nano Mater. 3 (10) (2020) 10057–10066, https://doi.org/10.1021/acsanm.0c02058.

[41] A. Di Bartolomeo, A. Pelella, X. Liu, F. Miao, M. Passacantando, F. Giubileo, A. Grillo, L. Iemmo, F. Urban, S. Liang, Pressure-tunable ambipolar conduction and hysteresis in thin palladium diselenide field effect transistors, Adv. Funct. Mater. 29 (29) (2019), 1902483, https://doi.org/10.1002/adfm.201902483.

[42] W. Zhang, J.-K. Huang, C.-H. Chen, Y.-H. Chang, Y.-J. Cheng, L.-J. Li, High-gain phototransistors based on a CVD MoS_2 monolayer, Adv. Mater. 25 (25) (2013) 3456–3461, https://doi.org/10.1002/adma.201301244.

[43] J.K. Gustafson, D. Wines, E. Gulian, C. Ataca, L.M. Hayden, Positive and negative photoconductivity in monolayer MoS_2 as a function of physisorbed oxygen, J. Phys. Chem. C 125 (16) (2021) 8712–8718, https://doi.org/10.1021/acs.jpcc.1c01550.

[44] X. Li, H. Zhu, Two-dimensional MoS2: properties, preparation, and applications, J. Mater. 1 (1) (2015) 33–44, https://doi.org/10.1016/j.jmat.2015.03.003.

[45] C. Lee, H. Yan, L.E. Brus, T.F. Heinz, J. Hone, S. Ryu, Anomalous lattice vibrations of single- and few-layer MoS_2, ACS Nano 4 (5) (2010) 2695–2700, https://doi.org/10.1021/nn1003937.

[46] E. Pollmann, L. Madauß, V. Zeuner, M. Schleberger, Strain in single-layer MoS2 flakes grown by chemical vapor deposition, in: Encyclopedia of Interfacial Chemistry, Elsevier, 2018, pp. 338–343, https://doi.org/10.1016/B978-0-12-409547-2.14175-7.

[47] S.E. Panasci, E. Schilirò, G. Greco, M. Cannas, F.M. Gelardi, S. Agnello, F. Roccaforte, F. Giannazzo, Strain, doping, and electronic transport of large area monolayer MoS_2 exfoliated on gold and transferred to an insulating substrate, ACS Appl. Mater. Interfaces 13 (26) (2021) 31248–31259, https://doi.org/10.1021/acsami.1c05185.

[48] E. Pollmann, L. Madauß, S. Schumacher, U. Kumar, F. Heuvel, C. Vom Ende, S. Yilmaz, S. Güngörmüs, M. Schleberger, Apparent differences between single layer molybdenum disulphide fabricated via chemical vapour deposition and exfoliation, Nanotechnology 31 (50) (2020), 505604, https://doi.org/10.1088/1361-6528/abb5d2.

[49] A.T. Neal, H. Liu, J.J. Gu, P.D. Ye, Metal contacts to MoS2: a two-dimensional semiconductor, in: 70th Device Research Conference, IEEE: University Park, PA, USA, 2012, pp. 65–66, https://doi.org/10.1109/DRC.2012.6256928.

[50] Z. Cheng, J.A. Cardenas, F. McGuire, S. Najmaei, A.D. Franklin, Modifying the Ni-MoS_2 contact interface using a broad-beam ion source, IEEE Electr. Device Lett. 37 (9) (2016) 1234–1237, https://doi.org/10.1109/LED.2016.2591552.

[51] C.D. English, G. Shine, V.E. Dorgan, K.C. Saraswat, E. Pop, Improved contacts to MoS_2 transistors by ultra-high vacuum metal deposition, Nano Lett. 16 (6) (2016) 3824–3830, https://doi.org/10.1021/acs.nanolett.6b01309.

[52] F. Urban, G. Lupina, A. Grillo, N. Martucciello, A. Di Bartolomeo, Contact resistance and mobility in back-gate graphene transistors, Nano Ex. 1 (1) (2020), 010001, https://doi.org/10.1088/2632-959X/ab7055.

[53] A. Di Bartolomeo, A. Grillo, F. Urban, L. Iemmo, F. Giubileo, G. Luongo, G. Amato, L. Croin, L. Sun, S.-J. Liang, L.K. Ang, Asymmetric Schottky contacts in bilayer MoS_2 field effect transistors, Adv. Funct. Mater. 28 (28) (2018), 1800657, https://doi.org/10.1002/adfm.201800657.

[54] A. Grillo, A. Di Bartolomeo, A current–voltage model for double Schottky barrier devices, Adv. Electron. Mater. 7 (2) (2021), 2000979, https://doi.org/10.1002/aelm.202000979.

[55] X. Wang, S.Y. Kim, R.M. Wallace, Interface chemistry and band alignment study of Ni and Ag contacts on MoS_2, ACS Appl. Mater. Interfaces 13 (13) (2021) 15802–15810, https://doi.org/10.1021/acsami.0c22476.

[56] J. Hong, Z. Hu, M. Probert, K. Li, D. Lv, X. Yang, L. Gu, N. Mao, Q. Feng, L. Xie, J. Zhang, D. Wu, Z. Zhang, C. Jin, W. Ji, X. Zhang, J. Yuan, Z. Zhang, Exploring atomic defects in molybdenum disulphide monolayers, Nat. Commun. 6 (1) (2015) 6293, https://doi.org/10.1038/ncomms7293.

[57] H. Qiu, T. Xu, Z. Wang, W. Ren, H. Nan, Z. Ni, Q. Chen, S. Yuan, F. Miao, F. Song, G. Long, Y. Shi, L. Sun, J. Wang, X. Wang, Hopping transport through defect-induced localized states in molybdenum disulphide, Nat. Commun. 4 (1) (2013) 2642, https://doi.org/10.1038/ncomms3642.

[58] C. Marquez, N. Salazar, F. Gity, J.C. Galdon, C. Navarro, R. Duffy, P. Hurley, F. Gamiz, Performance and reliability in back-gated CVD-grown MoS2 devices, Solid State Electron. 186 (2021), 108173, https://doi.org/10.1016/j.sse.2021.108173.

[59] A. Pelella, A. Grillo, F. Urban, F. Giubileo, M. Passacantando, E. Pollmann, S. Sleziona, M. Schleberger, A. Di Bartolomeo, Gate-controlled field emission current from MoS_2 nanosheets, Adv. Electron. Mater. 7 (2) (2021), 2000838, https://doi.org/10.1002/aelm.202000838.

[60] H. Kim, W. Kim, M. O'Brien, N. McEvoy, C. Yim, M. Marcia, F. Hauke, A. Hirsch, G.-T. Kim, G.S. Duesberg, Optimized single-layer MoS_2 field-effect transistors by non-covalent functionalisation, Nanoscale 10 (37) (2018) 17557–17566, https://doi.org/10.1039/C8NR02134A.

[61] A.-R. Jang, Tuning Schottky barrier of single-layer MoS2 field-effect transistors with graphene electrodes, Nanomaterials 12 (17) (2022) 3038, https://doi.org/10.3390/nano12173038.

[62] A. Di Bartolomeo, F. Urban, A. Pelella, A. Grillo, L. Iemmo, E. Faella, F. Giubileo, Electrical transport in two-dimensional PdSe2 and Mos2 nanosheets, in: 2020 IEEE 20th International Conference on Nanotechnology (IEEE-NANO), IEEE, Montreal, QC, Canada, 2020, pp. 276–281, https://doi.org/10.1109/NANO47656.2020.9183617.

[63] N. Kaushik, D.M.A. Mackenzie, K. Thakar, N. Goyal, B. Mukherjee, P. Boggild, D. H. Petersen, S. Lodha, Reversible hysteresis inversion in MoS2 field effect transistors, NPJ 2D Mater. Appl. 1 (1) (2017) 34, https://doi.org/10.1038/s41699-017-0038-y.

[64] J. Shu, G. Wu, Y. Guo, B. Liu, X. Wei, Q. Chen, The intrinsic origin of hysteresis in MoS_2 field effect transistors, Nanoscale 8 (5) (2016) 3049–3056, https://doi.org/10.1039/C5NR07336G.

[65] T. Knobloch, G. Rzepa, Y. Yu Illarionov, M. Waltl, F. Schanovsky, B. Stampfer, M. M. Furchi, T. Mueller, T. Grasser, A physical model for the hysteresis in MoS_2 transistors, IEEE J. Electr. Dev. Soc. 6 (2018) 972–978, https://doi.org/10.1109/JEDS.2018.2829933.

[66] F. Urban, F. Giubileo, A. Grillo, L. Iemmo, G. Luongo, M. Passacantando, T. Foller, L. Madauß, E. Pollmann, M.P. Geller, D. Oing, M. Schleberger, A. Di Bartolomeo,

Gas dependent hysteresis in MoS_2 field effect transistors, 2D Mater. 6 (4) (2019), 045049, https://doi.org/10.1088/2053-1583/ab4020.
[67] D.J. Late, B. Liu, H.S.S.R. Matte, V.P. Dravid, C.N.R. Rao, Hysteresis in single-layer MoS_2 field effect transistors, ACS Nano 6 (6) (2012) 5635–5641, https://doi.org/10.1021/nn301572c.
[68] H. Jawa, A. Varghese, S. Lodha, Electrically tunable room temperature hysteresis crossover in underlap MoS_2 field-effect transistors, ACS Appl. Mater. Interfaces 13 (7) (2021) 9186–9194, https://doi.org/10.1021/acsami.0c21530.
[69] M.Y. Chan, K. Komatsu, S.-L. Li, Y. Xu, P. Darmawan, H. Kuramochi, S. Nakaharai, A. Aparecido-Ferreira, K. Watanabe, T. Taniguchi, K. Tsukagoshi, Suppression of thermally activated carrier transport in atomically thin MoS2 on crystalline hexagonal boron nitride substrates, Nanoscale 5 (20) (2013) 9572, https://doi.org/10.1039/c3nr03220e.
[70] N. Ma, D. Jena, Charge scattering and mobility in atomically thin semiconductors, Phys. Rev. X 4 (1) (2014), 011043, https://doi.org/10.1103/PhysRevX.4.011043.
[71] N. Huo, Y. Yang, Y.-N. Wu, X.-G. Zhang, S.T. Pantelides, G. Konstantatos, High carrier mobility in monolayer CVD-grown MoS_2 through phonon suppression, Nanoscale 10 (31) (2018) 15071–15077, https://doi.org/10.1039/C8NR04416C.
[72] W.-C. Shen, R.-S. Chen, Y.-S. Huang, Photoconductivities in MoS2 nanoflake photoconductors, Nanosc. Res. Lett. 11 (1) (2016) 124, https://doi.org/10.1186/s11671-016-1331-y.
[73] O. Lopez-Sanchez, D. Lembke, M. Kayci, A. Radenovic, A. Kis, Ultrasensitive photodetectors based on monolayer MoS2, Nat. Nanotechnol. 8 (7) (2013) 497–501, https://doi.org/10.1038/nnano.2013.100.
[74] Y. Li, L. Li, S. Li, J. Sun, Y. Fang, T. Deng, Highly sensitive photodetectors based on monolayer MoS_2 field-effect transistors, ACS Omega 7 (16) (2022) 13615–13621, https://doi.org/10.1021/acsomega.1c07117.
[75] H. Şar, A. Özden, B. Yorulmaz, C. Sevik, N. Kosku Perkgoz, F. Ay, A comparative device performance assesment of CVD grown MoS2 and WS2 monolayers, J. Mater. Sci. Mater. Electron. 29 (10) (2018) 8785–8792, https://doi.org/10.1007/s10854-018-8895-5.
[76] D. Vaquero, V. Clericò, J. Salvador-Sánchez, E. Díaz, F. Domínguez-Adame, L. Chico, Y.M. Meziani, E. Diez, J. Quereda, Fast response photogating in monolayer MoS_2 phototransistors, Nanoscale 13 (38) (2021) 16156–16163, https://doi.org/10.1039/D1NR03896F.
[77] S. Ghosh, A. Winchester, B. Muchharla, M. Wasala, S. Feng, A.L. Elias, M.B. M. Krishna, T. Harada, C. Chin, K. Dani, S. Kar, M. Terrones, S. Talapatra, Ultrafast intrinsic photoresponse and direct evidence of sub-gap states in liquid phase exfoliated MoS2Thin films, Sci. Rep. 5 (1) (2015), 11272, https://doi.org/10.1038/srep11272.
[78] K. Czerniak-Łosiewicz, A.P. Gertych, M. Świniarski, J. Judek, M. Zdrojek, Time dependence of photocurrent in chemical vapor deposition MoS_2 monolayer – intrinsic properties and environmental effects, J. Phys. Chem. C 124 (34) (2020) 18741–18746, https://doi.org/10.1021/acs.jpcc.0c04452.
[79] A. Pelella, O. Kharsah, A. Grillo, F. Urban, M. Passacantando, F. Giubileo, L. Iemmo, S. Sleziona, E. Pollmann, L. Madauß, M. Schleberger, A. Di Bartolomeo, Electron irradiation of metal contacts in monolayer MoS_2 field-effect transistors, ACS Appl. Mater. Interfaces 12 (36) (2020) 40532–40540, https://doi.org/10.1021/acsami.0c11933.
[80] G. Dushaq, B. Paredes, J.-Y. Lu, M. Chiesa, M. Rasras, Tuning the photoluminescence of few-layer MoS_2 nanosheets by mechanical nanostamping for broadband optoelectronic applications, ACS Appl. Nano Mater. 3 (10) (2020) 10333–10341, https://doi.org/10.1021/acsanm.0c02235.
[81] H.J. Conley, B. Wang, J.I. Ziegler, R.F. Haglund, S.T. Pantelides, K.I. Bolotin, Bandgap engineering of strained monolayer and bilayer MoS_2, Nano Lett. 13 (8) (2013) 3626–3630, https://doi.org/10.1021/nl4014748.
[82] G. Sun, F. Li, T. Wu, L. Cong, L. Sun, G. Yang, H. Xie, A. Mauger, C.M. Julien, J. Liu, O_2 adsorption associated with sulfur vacancies on MoS_2 microspheres, Inorg. Chem. 58 (3) (2019) 2169–2176, https://doi.org/10.1021/acs.inorgchem.8b03300.
[83] R. Szoszkiewicz, Local interactions of atmospheric oxygen with MoS2 crystals, Materials 14 (20) (2021) 5979, https://doi.org/10.3390/ma14205979.
[84] B. Zhao, C. Shang, N. Qi, Z.Y. Chen, Z.Q. Chen, Stability of defects in monolayer MoS2 and their interaction with O2 molecule: a first-principles study, Appl. Surf. Sci. 412 (2017) 385–393, https://doi.org/10.1016/j.apsusc.2017.03.281.
[85] K. Wang, B. Paulus, Toward a comprehensive understanding of oxygen on MoS_2 : from reaction to optical properties, J. Phys. Chem. C 125 (35) (2021) 19544–19550, https://doi.org/10.1021/acs.jpcc.1c05473.
[86] S. Tongay, J. Zhou, C. Ataca, J. Liu, J.S. Kang, T.S. Matthews, L. You, J. Li, J. C. Grossman, J. Wu, Broad-range modulation of light emission in two-dimensional semiconductors by molecular physisorption gating, Nano Lett. 13 (6) (2013) 2831–2836, https://doi.org/10.1021/nl4011172.
[87] Y. Wang, Z. He, J. Zhang, H. Liu, X. Lai, B. Liu, Y. Chen, F. Wang, L. Zhang, UV illumination enhanced desorption of oxygen molecules from monolayer MoS2 surface, Nano Res. 13 (2) (2020) 358–365, https://doi.org/10.1007/s12274-020-2614-2.
[88] J. He, Y. Yang, Y. He, C. Ge, Y. Zhao, L. Gao, J. Tang, Low noise and fast photoresponse of few-layered MoS_2 passivated by MA_3 Bi_2 Br_9, ACS Photon. 5 (5) (2018) 1877–1884, https://doi.org/10.1021/acsphotonics.8b00129.
[89] A. Grillo, A. Di Bartolomeo, F. Urban, M. Passacantando, J.M. Caridad, J. Sun, L. Camilli, Observation of 2D conduction in ultrathin germanium arsenide field-effect transistors, ACS Appl. Mater. Interfaces 12 (11) (2020) 12998–13004, https://doi.org/10.1021/acsami.0c00348.
[90] Y.-C. Wu, C.-H. Liu, S.-Y. Chen, F.-Y. Shih, P.-H. Ho, C.-W. Chen, C.-T. Liang, W.-H. Wang, Extrinsic origin of persistent photoconductivity in monolayer MoS2 field effect transistors, Sci. Rep. 5 (1) (2015), 11472, https://doi.org/10.1038/srep11472.
[91] A. Di Bartolomeo, L. Iemmo, F. Giubileo, G. Luongo, F. Urban, A. Grillo, Persistent photoconductivity, hysteresis and field emission in MoS2 back-gate field-effect transistors, in: 2018 IEEE 13th Nanotechnology Materials and Devices Conference (NMDC), IEEE, Portland, OR, USA, 2018, pp. 1–2, https://doi.org/10.1109/NMDC.2018.8605928.
[92] J. Zhou, T. Järvinen, O. Pitkänen, Z. Kónya, A. Kukovecz, K. Kordas, Composites of ion-in-conjugation polysquaraine and SWCNTs for the detection of H_2S and NH_3 at Ppb concentrations, Nanotechnology 32 (18) (2021), 185502, https://doi.org/10.1088/1361-6528/abdf06.
[93] P.K. Sahu, M. Pandey, C. Kumar, S.S. Pandey, W. Takashima, V.N. Mishra, R. Prakash, Air-stable vapor phase sensing of ammonia in sub-threshold regime of poly(2,5-bis(3-tetradecylthiophen-2yl)Thieno(3,2-b)thiophene) based polymer thin-film transistor, Sens. Actuat. B Chem. 246 (2017) 243–251, https://doi.org/10.1016/j.snb.2017.02.063.
[94] J. Zhou, M. Bagheri, T. Järvinen, C. Pravda Bartus, A. Kukovecz, H.-P. Komsa, K. C. Kordas, $_{60}$ Br $_{24}$/SWCNT: a highly sensitive Medium to detect H $_2$ S via inhomogeneous carrier doping, ACS Appl. Mater. Interfaces 13 (49) (2021) 59067–59075, https://doi.org/10.1021/acsami.1c16807.
[95] R. Kozubek, M. Tripathi, M. Ghorbani-Asl, S. Kretschmer, L. Madauß, E. Pollmann, M. O'Brien, N. McEvoy, U. Ludacka, T. Susi, G.S. Duesberg, R.A. Wilhelm, A. V. Krasheninnikov, J. Kotakoski, M. Schleberger, Perforating freestanding molybdenum disulfide monolayers with highly charged ions, J. Phys. Chem. Lett. 10 (5) (2019) 904–910, https://doi.org/10.1021/acs.jpclett.8b03666.